

## Research Article

# High-Resolution Elevation Model of Lop Nur Playa Derived from TanDEM-X

Yuyang Geng <sup>1,2,3</sup>, Yun Shao <sup>1,2</sup>, Tingting Zhang <sup>1,3</sup>, Huaze Gong<sup>1,3</sup> and Lan Yang<sup>4</sup>

<sup>1</sup>*Institute of Remote Sensing and Digital Earth, Chinese Academy of Sciences, 100101, China*

<sup>2</sup>*University of Chinese Academy of Science, 100049, China*

<sup>3</sup>*Laboratory of Target Microwave Properties, Deqing Academy of Satellite Applications, 313200, China*

<sup>4</sup>*China University of Geosciences, 100083, China*

Correspondence should be addressed to Tingting Zhang; zhangtt@radi.ac.cn

Received 15 February 2019; Revised 30 May 2019; Accepted 10 July 2019; Published 18 August 2019

Guest Editor: Hyung-Sup Jung

Copyright © 2019 Yuyang Geng et al. This is an open access article distributed under the Creative Commons Attribution License, which permits unrestricted use, distribution, and reproduction in any medium, provided the original work is properly cited.

In this paper, a digital elevation model (DEM) was produced for Lop Nur playa produced with the data from TanDEM-X mission. The spatial resolution is 10 m. It covers an area of 38,000 km<sup>2</sup> for orthometric height from 785 m to 900 m above sea level, which is composed of 42 interferometric synthetic aperture radar (InSAR) scenes. A least-square adjustment approach was used to reduce the systematic errors in each DEM scene. The DEM produced was validated with data from other sensors including Ice, Cloud, and land Elevation Satellite (ICESat) Geoscience Laser Altimeter System (GLAS) and aerial Structure-from-Motion (SfM) DEM. The results show that global elevation root mean square error to GLAS is 0.57 m, and the relative height error to SfM DEM in complicated terrain is 3 m. The excellent height reliability of TanDEM InSAR DEM in Lop region was proved in this paper. A reliable high-resolution basic topographic dataset for researches of Lop Nur was provided.

## 1. Introduction

Lop Nur used to be the terminal lake of all rivers in the Tarim Basin but had been desiccated since 1973 [1]. The remaining playa is located in the northwestern China between latitude 39°N and 41° and longitude 89°E and 92°E. It is important for studying the interaction between ancient human activities and paleoclimate change, especially after the discovery of Loulan city of Chinese Han Dynasty in 1901 by Hedin [2]. Meanwhile, his proposed wandering lake theory [2], which believed the ancient Lake Lop Nur would alternate its lake basin between depressions in this region according to elevation difference derived from erosion and accumulation [3], had been controversial among the international Earth science community for nearly a century [4]. The debate and other paleo-environment researches, such as determination of the lake boundary, discovery of paleo river channel, and building a 3D hydrodynamic model, all require high-resolution full-coverage topographic materials [5, 6].

Although some topographic surveys have been conducted, a reliable digital elevation model (DEM) over Lop

Nur playa is still absent. The primitive leveling surveys [1] distributed sparsely in the playa with limited height accuracy. Afterwards Differential Global Positioning System (DGPS) measurements were completed in the desiccated lake basin [7], while Ice, Cloud, and land Elevation Satellite (ICESat) Geoscience Laser Altimeter System (GLAS) elevation was estimated to be more reliable than that of DGPS in Lop Nur playa [8]. Although the height accuracy of both reached several decimeters, the spatial distribution of DGPS and GLAS was confined either along existing roads due to the reaching accessibility of vehicles or along tracks of the satellite orbits. As the DGPS and GLAS measurements show, the Lop Nur playa is quite flat with an elevation difference of 5 m from the center to the edge, and a slope of only 0.2‰. The smooth terrain requires an excellent relative height accuracy of DEM to reveal its topography. Global DEM products SRTM [9, 10] and GDEM [11, 12] both cover the Lop Nur playa, but neither the spatial resolution nor height accuracy is appropriate to interpret the fluvial landforms and the topography of lake basin.

TanDEM-X mission is designed to generate a global DEM with unprecedented accuracy [13] as the basis for

various applications, such as landslide tracking [14], glacier changing [15–17], vegetation evaluating [18, 19], lava flow estimating [20, 21], and permafrost monitoring [22]. The TanDEM-X mission consists of twin satellites TerraSAR-X and TanDEM-X working on bistatic interferometry mode, which is characterized by the illumination of a target region on the ground by one transmitter and the simultaneous acquisition of the backscattered signals with two receivers [23]. This simultaneous acquisition avoids possible influences from temporal decorrelation and atmospheric disturbances [13]. The relative height accuracy is 2 m when slope is less than 20% [24]. Moreover, TanDEM-X acquisitions in StripMap mode have a ground spatial resolution of 2–3 m, which is much better than past SAR sensors previously cited, e.g., SIR-C (12.5 m), TOPSAR (10 m), ERS-1/2 (30 m), or ALOS/PALSAR (10 m). The high spatial resolution and the bistatic mode of the TanDEM-X mission therefore provide unprecedented opportunities to produce high-resolution DEM to characterize the elevation varying of Lop Nur playa.

This study aims to (1) eliminate remaining system errors with the least-square adjustment approach; (2) derive DEM of Lop Nur playa with a spatial resolution of 10 m using TanDEM-X/TerraSAR-X interferometric synthetic aperture radar (InSAR) image pairs; (3) compare the DEM results with ICESat GLAS footprints, aerial Structure-from-Motion (SfM) DEM, and SRTM DEM.

## 2. Materials and Methods

**2.1. TanDEM-X Data.** 42 TanDEM-X/TerraSAR-X Coregistered Single look Slant range Complex (CoSSC) [25] image pairs from the TanDEM-X mission, which is supported by DLR TanDEM-X science coordination project of OTHER6906 and ATL\_HYDR7333, are used to generate the target DEM. Table 1 lists the characteristics of image pairs used in this paper. They are all acquired on ascending orbit with right looking direction, and in HH polarization. The data are obtained during 2011 to 2015.

The preadjustment DEMs are processed in InSAR TanDEM-X Bistatic DEM Workflow module of SARscape© 5.2.1, where Goldstein filter [26] and Delaunay Minimum Cost Flow (MCF) [27] are assigned for noise reduction and phase unwrapping, respectively. A detailed description of the full processing of SAR data with SARscape© is provided by Sahraoui et al. [28]. The licenses of SARscape© and ENVI© are granted by Institute of Remote Sensing and Digital Earth, CAS. As the geo-location accuracy can be assumed as at least 10 m [29], the output resolution of geocoded DEM could be approximately equivalent to it. Thus, the DEM was obtained with a ground spatial posting of 0.3 arc sec, which, in the studied area, corresponds to 7 m in longitude and 9 m in latitude. From this value and according to the range/azimuth resolution of the radar images, a multilooking factor of 4 is applied in range and in azimuth to the initial radar images to reduce the speckle. In the interferometric processing, elevation is only calculated for pixels that have a coherence value larger than 0.25 to prevent aberrant values

in steep slopes where layover and shadowing effects are present.

Although instrument and system calibrations have been carried out to produce CoSSC [30], offsets of few meters and tilts in range and azimuth of some decimeters still remained [31], which means these errors should be estimated before mosaic.

**2.2. ICESat GLA14 Elevation Data.** The data of ICESat mission was used as the height truth value for both adjustment and validation. The GLAS on ICESat is a laser altimeter system that measures the Earth surface with a footprint of about 70 m. The footprints were successfully used as ground control points to generate DEM [23, 32, 33] for its reliable vertical accuracy of average 13 cm [34–37]. It operated from 2003 to 2009. GLA14 is the global land surface altimetry product of ICESat mission [34]. In this paper, to remove the noise in GLA14, selection rules considering cloud, attitude quality mark, energy saturation parameters, and the waveform characteristic [38] were executed to screen data. In particular, the waveform characteristic thresholds guarantee that the terrain variation in the footprint would be less than 1 meter [37]; thus the GLAS GCPs could be adaptive to InSAR DEM although their spatial resolutions are different. The data ellipsoid was transformed from TOPEX/Poseidon to WGS84 [39]. The ellipsoidal height was amended to orthometric height by geoidal undulation derived from the Earth Gravitational Model EGM2008 [40, 41]. 18,440 qualified GLAS GCPs were obtained after preprocessing, where half of them were randomly chosen as adjustment control points and the remaining were taken as the vertical height uncertainty check points.

**2.3. Aerial SfM DEM.** Aerial photogrammetry SfM [42–45] is a burgeoning technology to obtain high-resolution DEM in a small scale. To evaluate the local performance of the resulting InSAR DEM, the ruined fort LK (89.667987°E, 40.094285°N) [46] near Lop Nur playa is taken as a validation site. In 2018, aerial photogrammetry SfM field work was conducted to obtain a 3D model of the ancient fort. Aerial photos were taken by DJI Phantom 3 Pro in 30 meters above land, with more than 80% overlay of an approximately 200 x 200 m area covering the fort ruin. Total of 456 photos were aligned to generate DEM within spatial resolution of 2 centimeters in PhotoScan©. A detailed PhotoScan© workflow was described by Johnson et al. [47]. The educational license of PhotoScan© is granted by Agisoft.

**2.4. Adjustment Approach for InSAR DEM.** Since there are systematic errors in TanDEM-X DEM, majorly resulting from baseline estimation error, a polynomial function model [31] was used for least square adjustment, as follows:

$$g(p, x, y) = a_0 + a_1 \cdot x + a_3 \cdot y \quad (1)$$

where  $g$  is the error function model;  $x$  is the position along the azimuth direction;  $y$  is the position along the ground range direction;  $p = a_0, a_1, b_1$ , unknown error parameters;  $a_0$

TABLE 1: List of TanDEM-X COSSC used in this paper.

Date Y/M/D	Item ID	Center Latitude [°]	Center Longitude [°]	Mean Incidence [°]	Perpendicular Baseline [m]	Ambiguity Height [m]	Average Coherence
2011/3/8	1012680_018	40.689777	90.288025	46.14	-385.569	20.743	0.86
2011/5/24	1025019_002	40.616318	89.671165	42.58	320.650	22.19	0.71
2011/5/30	1025014_018	40.176941	91.918129	42.55	316.811	22.431	0.57
2011/5/30	1025014_020	41.054401	91.724747	42.52	315.917	22.484	0.88
2011/7/7	1024959_020	40.215164	90.080551	44.47	-300.385	25.209	0.83
2011/7/7	1024959_019	39.776711	90.176781	44.48	-300.599	25.196	0.85
2011/7/7	1024959_021	40.654144	89.988625	44.46	-300.117	25.226	0.77
2011/9/6	1043725_011	40.132442	91.573662	40.37	271.978	24.306	0.68
2011/9/6	1043725_012	40.514584	91.486214	40.36	271.686	24.327	0.88
2011/9/11	1025040_020	40.860825	88.917313	38.16	-268.049	22.893	0.87
2011/9/11	1025040_019	40.527100	88.993256	38.17	-268.300	22.877	0.66
2011/9/17	1021900_001	40.682053	91.474815	40.50	-270.020	24.597	0.88
2011/9/17	1021900_002	41.011890	91.401062	40.49	-269.795	24.613	0.88
2011/10/14	1042892_008	40.574436	89.341232	40.51	271.923	24.426	0.69
2011/11/22	1041891_010	40.489090	90.843994	36.08	219.263	26.012	0.85
2011/11/22	1041891_009	40.048294	90.931931	35.98	219.318	25.907	0.84
2011/12/3	1041582_014	40.442974	90.512253	33.61	-214.507	24.335	0.89
2011/12/3	1041582_013	40.004536	90.619080	33.63	-214.489	24.347	0.90
2012/8/17	1081781_004	40.188587	89.874321	43.21	-431.237	16.853	0.73
2012/8/17	1081781_003	39.748863	89.961990	43.16	-431.962	16.797	0.83
2012/10/6	1099741_002	40.942863	90.871582	36.95	-377.503	15.589	0.91
2012/10/22	1084167_003	39.667889	89.334038	39.15	-366.022	17.333	0.77
2012/10/22	1084167_002	39.228661	89.430214	39.08	-366.702	17.257	0.89
2012/10/28	1080470_002	40.899006	90.546562	34.59	-354.063	15.282	0.92
2012/11/24	1107934_002	39.627182	89.014275	36.97	385.790	16.082	0.73
2012/11/24	1107934_001	39.187695	89.097855	36.84	385.714	16.014	0.86
2013/1/24	1104443_004	40.529350	91.163483	38.28	-268.466	22.945	0.90
2013/1/24	1104443_003	40.090889	91.266251	38.29	-268.374	22.96	0.77
2013/1/24	1104443_005	40.968224	91.063660	38.26	-268.439	22.94	0.89
2013/1/24	1104443_004	40.529350	91.163483	38.28	-268.466	22.945	0.90
2013/4/5	1130615_005	40.589912	89.461823	41.28	375.776	18.135	0.73
2013/4/5	1130615_003	39.712265	89.656067	41.30	377.634	18.054	0.85
2013/4/5	1130615_004	40.150890	89.557449	41.29	376.716	18.094	0.66
2014/1/11	1171778_002	40.201839	88.838333	19.28	-82.656	33.589	0.80
2014/1/11	1171778_003	40.640186	88.722717	19.25	-81.492	34.028	0.85
2014/1/11	1171778_001	39.783157	88.948822	19.30	-83.777	33.178	0.85
2014/2/2	1173379_001	39.854599	89.217354	21.93	-101.314	31.485	0.86
2014/2/2	1173379_002	40.244377	89.115845	21.90	-100.127	31.826	0.79
2014/2/24	1191146_002	40.561501	89.505882	24.43	-125.332	28.685	0.79
2014/2/24	1191146_001	39.897343	89.497055	24.45	-128.733	28.386	0.87
2015/9/8	1312660_002	39.961605	90.337814	31.25	-1959.970	2.437	0.78
2015/9/8	1312660_003	40.400295	90.231071	31.23	-1948.710	2.45	0.76

denotes offset;  $a_1$  denotes tilt in azimuth;  $a_3$  denotes tilt in range.

The data process workflow was shown in Figure 1. Due to the sparse distribution of GLA14 (Figure 2) in Lop Nur playa,

how to select the primary DEMs for adjustment is a problem. The primary DEMs are picked up manually according to the conditions: (a) there are at least 2 tracks of GLA14 in the DEM scene; (b) the GLA14 GCPs distribute throughout the DEM

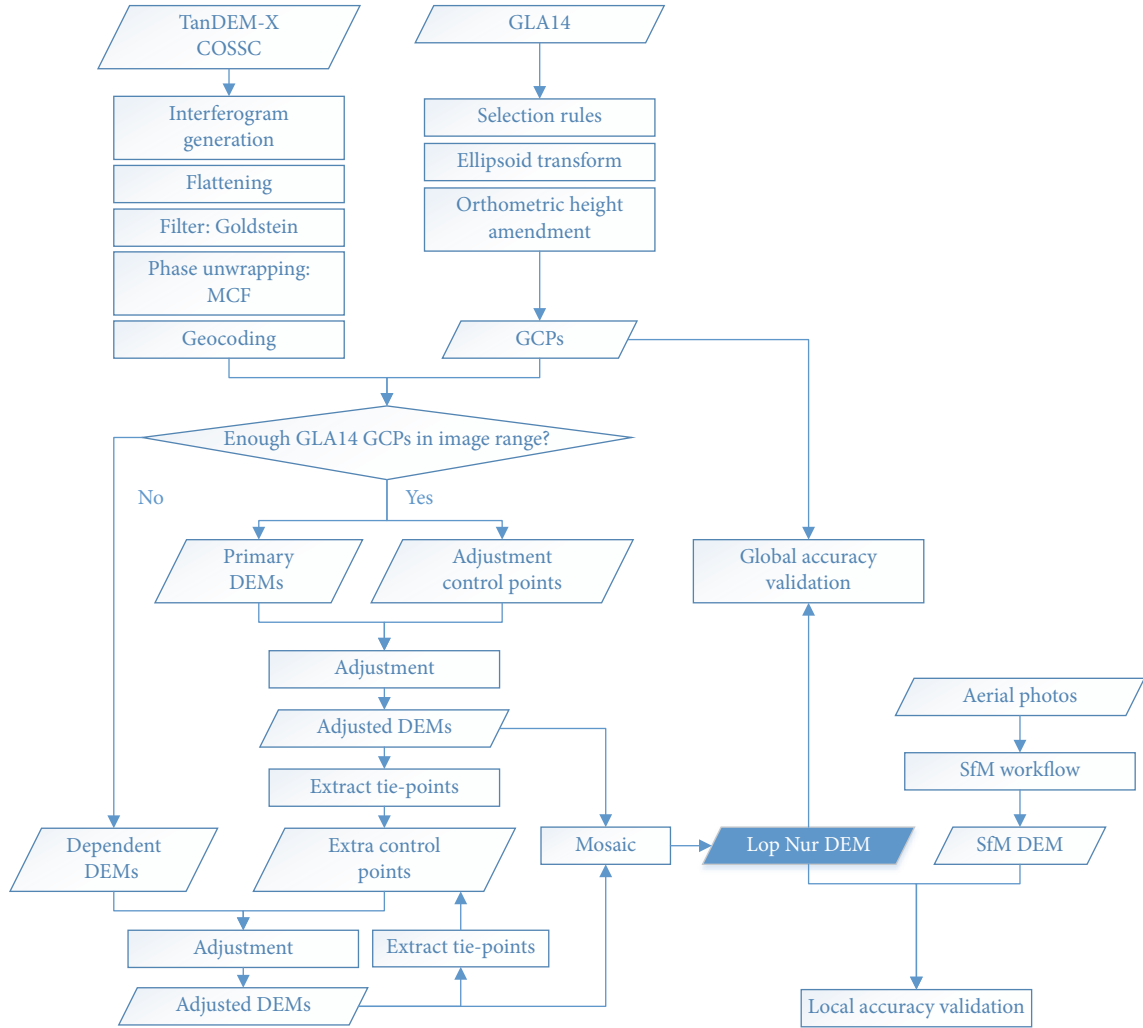


FIGURE 1: The workflow of DEM generation.

region as X shape, V shape, or parallel lines (Figure 2). GLA14 GCPs can be the height truth value for these selected DEMs, while the rest of DEMs depend on the tie-points extracted from the adjusted DEMs. Only part of the GLA14 GCPs was valid for adjustment, and the rest of them were used for height validation. Tie-points were extracted manually from the overlap region of adjacent adjusted DEMs. In order to reduce the influence of geo-location bias between DEMs, tie-points were selected on relatively flat terrain. Since the salt crust protects the playa surface from wind erosion, the terrain was assumed to be stable during the TanDEM-X acquisition period.

A block adjustment approach was applied to generate global TanDEM-X DEM [23]. Since the number of DEM scenes was only 42, a simplified least-square adjustment approach was used in this paper. For the primary DEMs, the observation equation is as follows:

$$\Delta\hat{H}_{GLA14,I} = g_I(\hat{p}, x, y) \quad (2)$$

where I is the index of DEM;  $\Delta\hat{H}_{GLA14,I}$  is the adjusted height difference between GLA14 GCPs and primary DEM.

For the dependent DEMs, the observation equation would be as follows:

$$\Delta\hat{H}_{J,K} = g_K(\hat{p}, x, y) - g_J(p, x, y) \quad (3)$$

where J is the index of adjusted DEM; K is the index of dependent DEM;  $\Delta\hat{H}_{J,K}$  is the adjusted height difference between dependent DEM and adjusted DEM.

Combining with GLA14 GCPs and tie-points, the estimated offsets and tilts of every DEM can be derived successively. To decrease the residual error between adjacent adjusted DEMs, averaging on the overlap region was applied in mosaic. 42 adjusted TanDEM-X DEM scenes were mosaicked to produce the Lop Nur playa DEM.

### 3. Results

The coherence parameter is an indicator of the stability of the ground targets. Generally, it is a function of geometric and temporal decorrelation between the two acquisitions, and it ranges from 0 (unstable) to 1 (highly stable). In the case of

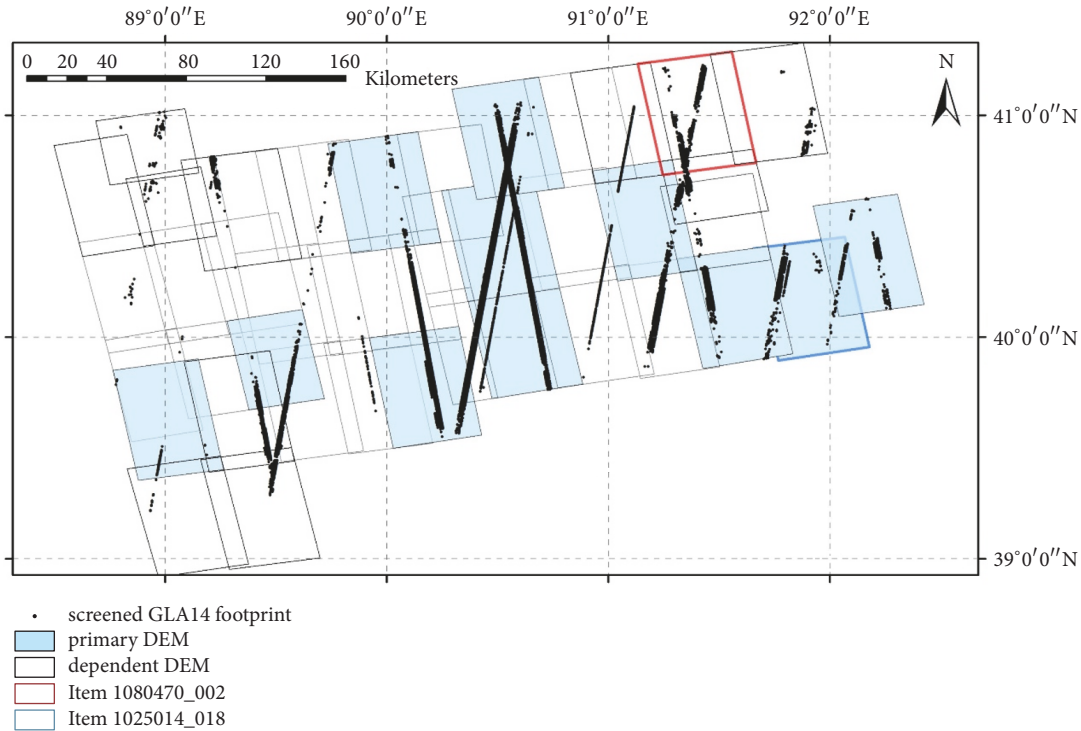


FIGURE 2: The primary DEMs, dependent DEMs, and screened GLA14 footprints. Images with minimum and maximum coherence were marked by different color.

bistatic interferometry, as temporal decorrelation is reduced, coherence is mainly dependent on the SAR hardware performance. Average coherence of item 1025014\_018 is minimum while that of item 1080470\_002 is maximum, whose coherence and interferogram were illustrated in Figure 3.

The result TanDEM-X DEM is presented in Figure 4. Although differences between adjacent DEMs were reduced by averaging, steps in the mosaicked DEM occurred partly. The residual error histogram (Figure 5) shows that the errors distribute more intensively in the mean value of  $\sim 0$  than the normal distribution. The global Root Mean Square Error (RMSE) of the DEM is 0.57 m, which is in the range of TanDEM-X DEM accuracy specification of 2 m when slope is less than 20% [13]. The InSAR DEM difference to GLA14 was projected on the tinting DEM to present the spatial features (Figure 4). The orthometric height of the resulting Lop Nur DEM is from 785 m above sea level (asl) to 900 m asl, which covers an area of around 35,000 km<sup>2</sup>.

On one hand, it would be appropriate to compare the global performance of TanDEM-X DEM and SRTM DEM in the study region. SRTM was the previous generation global interferometric DEM [48, 49], whose absolute height error was estimated at several meters with a spatial resolution of 3 arc sec ( $\sim 90$  m) in Eurasia [50]. In Figure 6, SRTM was rendered with the same color ramp with Figure 4, where the height error to GLA14 GCPs was also projected. The size of each error point was in direct proportion to the absolute value of its error with the same ratio of Figure 4. The error histogram of SRTM to GLA14 GCPs was shown in Figure 7. The mean value was 3.04 m and the RMSE was 1.74 m.

On the other hand, it is proper to validate the local performance of TanDEM-X DEM referencing to the aerial DEM. The aerial SfM DEM is in a spatial resolution of 2 cm with relative elevation accuracy estimated at the order of decimeter [44]. Five points in LK (location see Figure 6) were selected for quantitative comparisons, and the results were summarized in Table 2. Since they are in different elevation systems, it makes sense to compare the relative height rather than the absolute height. The flat ground to the east of the ruined fort is taken as the local base height (Figure 6).

#### 4. Discussion

Favorable coherence is crucial for interferometry. Item 10804700\_002 is in the north of the study area (Figure 2). The landform is mainly mountain in the north of this image and solid salt crust in the south. Although the terrain varies in mountains (Figure 3(c)), the coherence is significantly high. Coherence in some parts of the mountains is relatively low at about 0.5 due to shadowing effects. The coherence of salt crust is also high. Item 1025014\_018 is in the east of our region (Figure 2). The landforms are mountains and salt crust in the north of this image just like item 10804700\_002, where the coherence is also near 1. In the north of item 1025014\_018, the landform is desert. Due to the volume scattering of sand, the volume decorrelation effects decreased the coherence dramatically [51]. Similar volume decorrelation effects occur in other images, such as items 1130615\_004 and 1043725\_011, which makes the average coherence being lower than the others (see Table 1). However, in the western side of sand

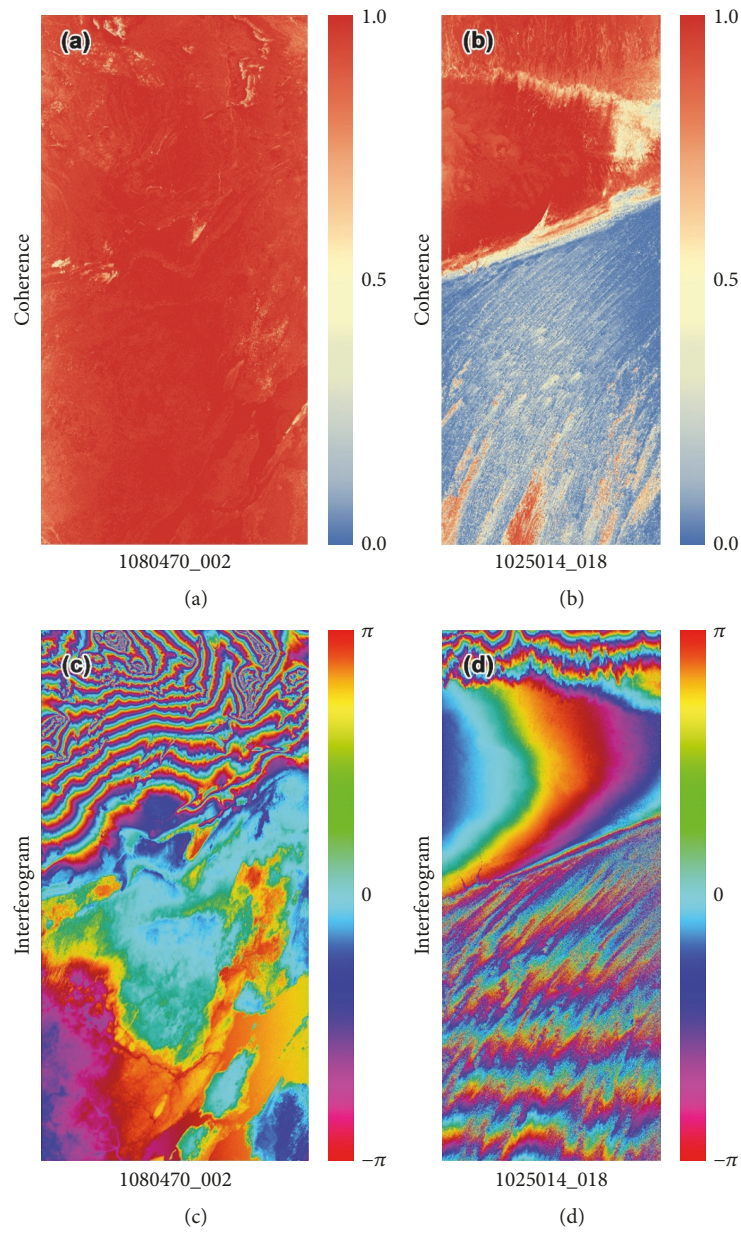


FIGURE 3: Coherence of (a) item 1080470\_002, (b) item 1025014\_018, and interferogram of (c) item 1080470\_002 and (d) item 1025014\_018.

TABLE 2: Relative elevation differences of the two DEMs.

Site	InSAR elevation [m]	SfM elevation [m]	InSAR relative elevation [m]	SfM relative elevation [m]	Error [m]
Reference Zero Height	793.6	791.739	0	0	\
NE Wall	800	799.177	6.4	7.438	-1.038
SW Wall	799.8	800.775	6.2	9.036	-2.836
SE Wall	797.4	795.837	3.8	4.098	-0.298
Northern Depression	793.6	790.307	0	-1.432	1.432
Southern Depression	795.8	791.679	2.2	-0.06	2.26

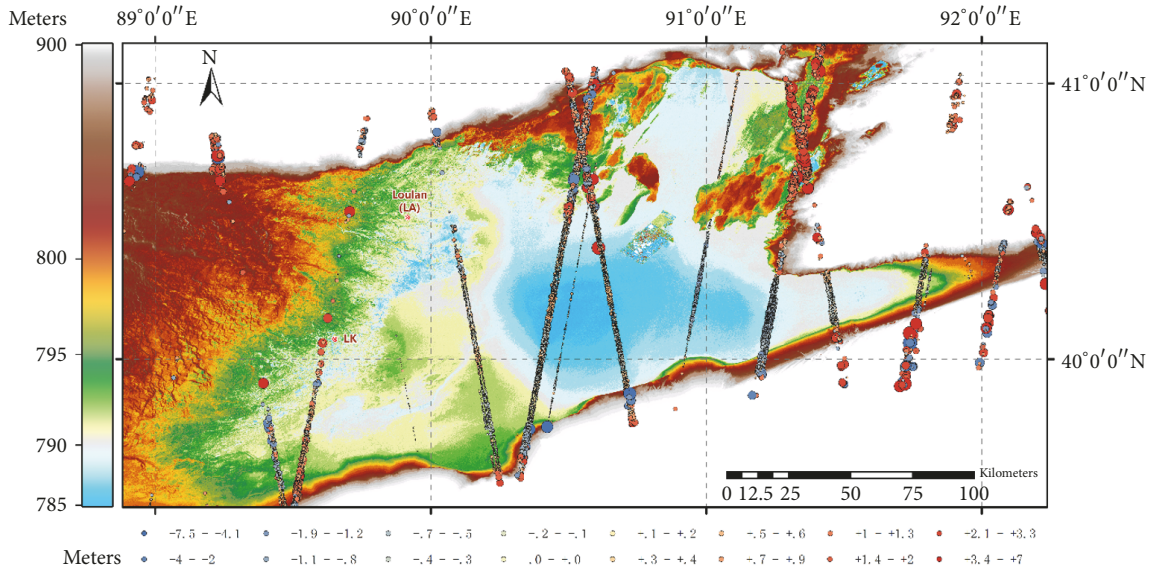


FIGURE 4: TanDEM-X DEM and the error distribution. The size of each error point is in direct proportion to the absolute value of its error, and its color represents its magnitude.

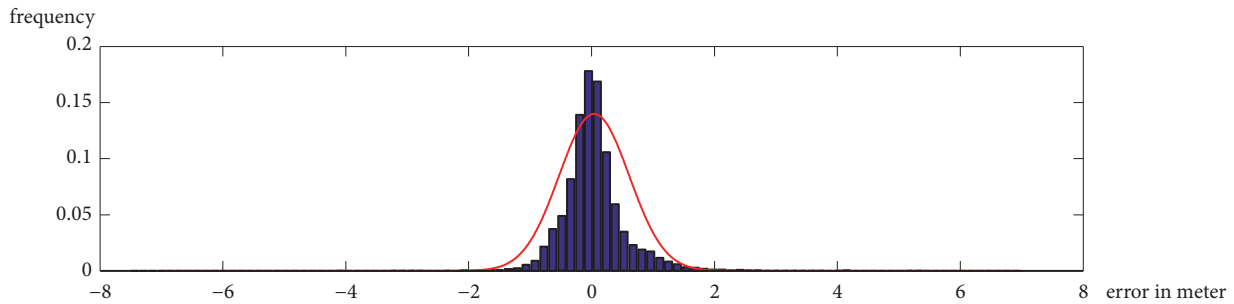


FIGURE 5: Histogram of TanDEM-X DEM height error to screened GLA14 footprints, with normal distribution fit line in red.

dunes which face the satellites, the coherence is relatively high at approximate or greater than 0.5. The local reliable features ensure interferogram available for further terrain inversion (Figure 3(d)).

The phase unwrapping method depends on the coherence features in the study region. There are three optional phase unwrapping methods in SARscape© 5.2.1, which are Region Growing, Minimum Cost Flow, and Delaunay Minimum Cost Flow, respectively.

(1) Region Growing is suggested to avoid setting a high coherence threshold in order to limit the possibility of introducing erroneous phase jump, like the unwrapping islands, in the output unwrapped phase image.

(2) Minimum Cost Flow should be adopted when the unwrapping process becomes difficult due to the presence of large areas of low coherence or other growing limiting factors; in such cases the Minimum Cost Flow algorithm enables obtaining better results than using the Region Growing method. This approach considers a square grid all over the image pixels. All pixels whose coherence is lower than the unwrapping coherence threshold are masked out.

(3) Delaunay Minimum Cost Flow is the same approach of the previous method, with the only difference that the grid does not necessarily cover all image pixels, but only those above the unwrapping coherence threshold. Moreover, it adopts the Delaunay triangular grid instead of square one. As a result, only the points with good coherence are unwrapped, without any influence from the low coherence pixels. It is especially useful when there are several areas of low coherence distributed throughout the image; in such case the other unwrapping approaches would eventually produce phase islands/jumps, while the Delaunay approach is able to minimize these jumps, which is the reason why Delaunay Minimum Cost Flow was chosen as the phase unwrapping method in this study.

However, the phase unwrapping error, including other error sources, still existed in resultant DEM. Referring to GLA14, errors in the eastern playa were small, usually less than 1 m, while the errors in the marginal desert, mountain, and Yordan region were sometimes significant. One of the possible reasons was that the geo-location of them was not rigorously aligned, or spatial scale of TanDEM-X DEM (10 m)

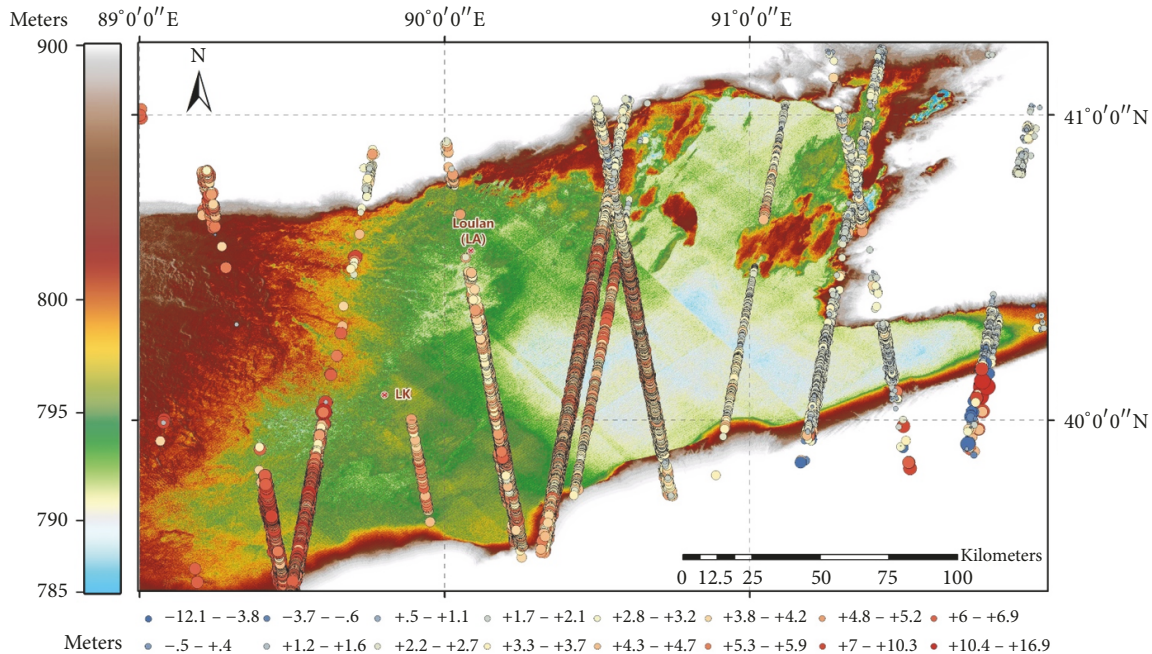


FIGURE 6: SRTM DEM and the error distribution. The size of each error point is in direct proportion to the absolute value of its error with the same ratio of Figure 4, and its color represents its magnitude.

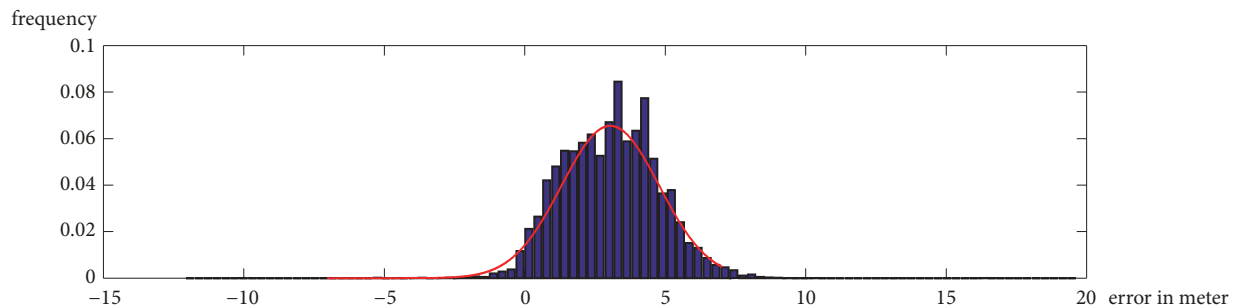


FIGURE 7: Histogram of SRTM DEM height error to screened GLA14 footprints, with normal distribution fit line in red.

did not match that of GLA14 (~70 m), so the elevation difference would be dramatic if the local terrain varies sharply, such as in the mountain and Yarden region. Besides, the volume scatter in desert could result in decoherence, which reduced the accuracy of phase unwrapping. Previous research showed that the high-frequency noise-like phase errors were usually below 1 m [31]. The RMSE of 0.57 m between resultant DEM and GLA14 indicated that the remnant errors are smaller than 1 m. On all accounts, the DEM was accurate enough to tint with a 1-m color ramp interval.

The visual performance of TanDEM-X DEM (Figure 4) was greater than SRTM DEM (Figure 6). There were some obvious northwest-southeast artifacts in SRTM DEM. Due to the insufficient spatial resolution and height accuracy, SRTM DEM presented the rougher terrain variations than TanDEM-X. More precisely, the spatial resolution of TanDEM-X DEM 0.3 arc sec was one order of magnitude higher than that of SRTM DEM 3 arc sec, and the standard deviation of the error reduced by a factor of 3, with a value

of 0.57 m for TanDEM-X (Figure 5), against 1.74 for SRTM (Figure 7). In Lop Nur plays, TanDEM-X DEM was more reliable than previous SRTM DEM.

Locally, the TanDEM-X DEM presented roughly the topography features of the ruined ramparts (Figure 8(a)). The relative heights of three points on the tops of the ramparts were all underestimated, which were higher than the assigned base height, and the difference was up to -2.8 m at the SW Wall (Table 2). A 20-m (2-pixel) displacement at the SE Wall was observed, which could result from the layover effect of the SAR system. The relative elevation of the two depressions inside the ruin was also underrated, even the depression characteristics were hardly recognized. Regardless, the worst relative error in such complicated terrain could be evaluated as 3 m, as shown in Table 2. The difference might be ascribed to the limitations of the radar system. On one hand, the 10-m resolution of InSAR DEM limits its spatial availability compared to SfM DEM. On the other hand, both walls and depressions are isolated islets with striking slope on their

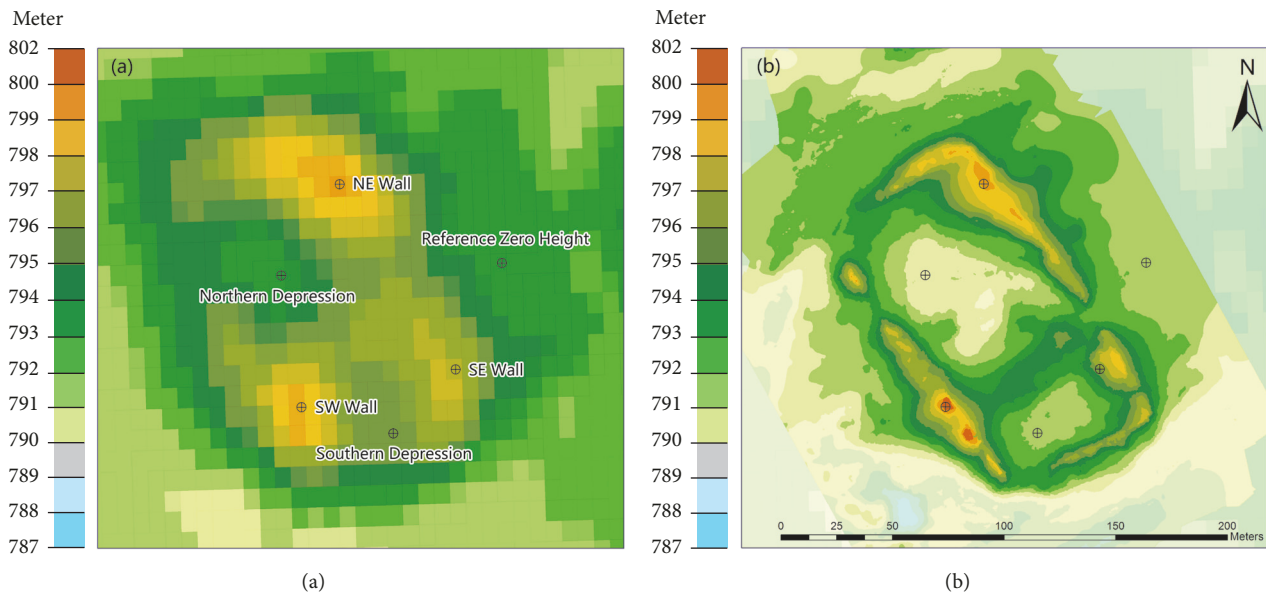


FIGURE 8: Comparison of DEM from different resources. (a) TanDEM-X DEM; (b) aerial SfM DEM. Color ramp is the same as that in Figure 3. Both are projected on WGS84 UTM Zone 45N.

margin, where the interferometric fringes would discontinue easily on an interferogram [52]. Hence, it requires us to be cautious when interpreting local isolated landforms. In any case, the relative height accuracy of 3 m was in the range of TanDEM-X DEM specification (4 m when slope > 20%) [13]. Although TanDEM-X DEM was not as accurate as aerial SfM DEM in both horizontal and vertical dimensions, its pivotal superiority was the full coverage of Lop Nur playa with a relatively reliable precision. It could be hardly to achieve an aerial SfM DEM throughout the study region in consideration of the amount of work. Besides, it was also difficult to find homologous points for SfM in homogeneous landforms (salt crust, desert, etc.). In current stage, spaceborne InSAR was the most proper way to derive a full-coverage DEM for Lop Nur playa.

The latest high-resolution TanDEM-X DEM could contribute to the paleo-environment and anthropology researches around Lop Nur playa. Previously, it was believed that there were only two main inflowing riverways for lake Lop Nur [1]. One was along the north of the Tarim Basin (region A in Figure 9), while the other was in the southeast of lake (region B in Figure 9). A wide riverway (region C in Figure 9) in the middle of the known riverways could be interpreted from the resultant DEM. Especially in the upstream of this riverway, a depression (region D in Figure 9) to the southeast of Loulan ruin could be identified, which was the Loulan depression relating with the evolution of ancient Lop Nur lake [2]. There were several hydrological channels in Loulan depression. Region C and Loulan depression might be used to be a near-lake wetland and affect the daily lives of residents in Loulan city, according to its geographical location. Geometry society paid little attention to these areas due to insufficient topographic data before. Besides, the altitude of the ancient ruins, channels and basins, could

also be an important clue to investigate the relationship between human beings and nature. A key strategy was that the lake surface level could not be higher than the altitude of the ancient ruins when these ruin cities were prosperous. It might be a novel evidence for understanding sediment profiles in Lop Nur.

## 5. Conclusions

This paper describes the derivation of a highly accurate DEM from TanDEM-X CoSSC images of Lop Nur playa via a least-square adjustment approach.

The resultant DEM covers an area of around 35,000 km<sup>2</sup> and has a horizontal resolution of 0.3 arc sec (~10 m) and a height accuracy of 0.57 m, representing the most accurate DEM in Lop Nur playa until now. The horizontal spatial resolution of the derived DEM is one magnitude higher than that of SRTM DEM, and the height accuracy is improved by a factor of 3. Validation of the derived DEM demonstrates its reliability for complicated terrains though it is not as good as for the flat region.

This highest quality DEM derived for Lop Nur can provide a basic material for general paleo-environment researches. A newfound river mouth of Lop Nur near Loulan ruin is interpreted from the resultant DEM. More field work in this area will be expected to reveal the relations between anthropology and nature.

## Data Availability

GLA14 data used to support the findings of this study have been deposited in the National Snow & Ice Data Center website (<https://nsidc.org/data/icesat/>). TerraSAR-X/TanDEM-X CoSSC and derived DEM used to support

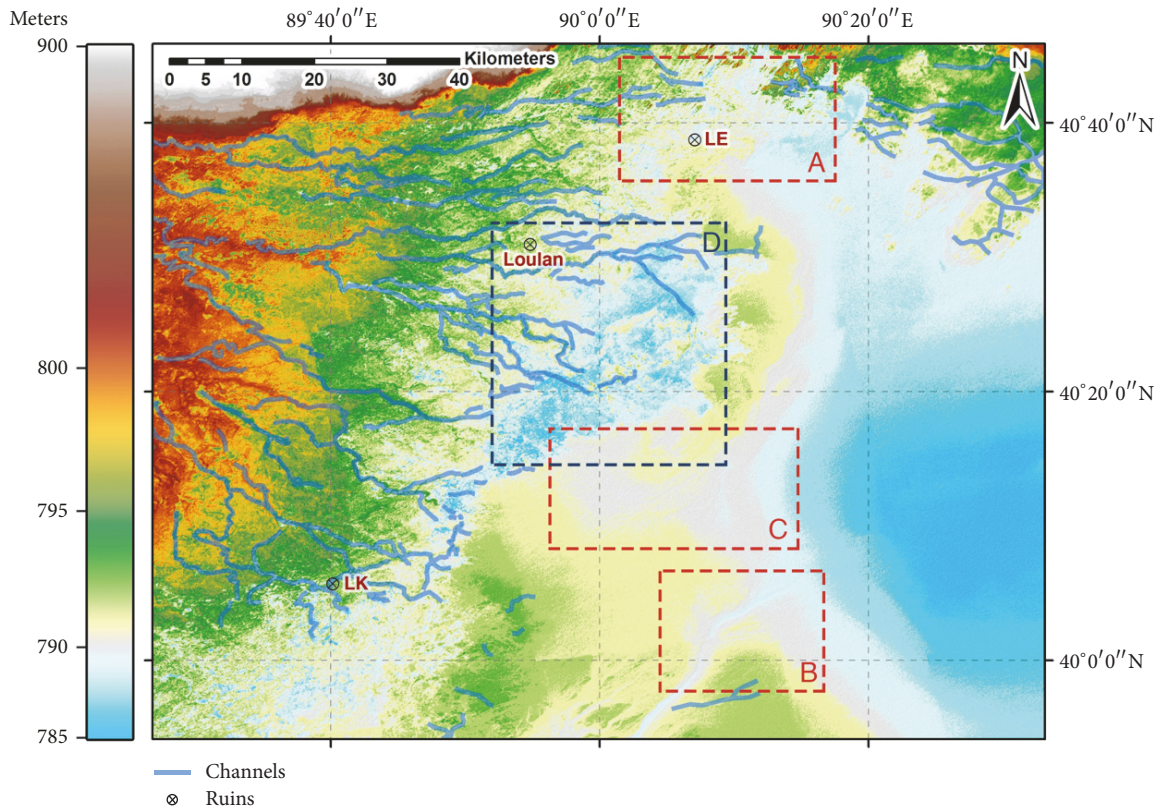


FIGURE 9: Interpretation of the TanDEM-X DEM. The known ruin ancient forts, LE, Loulan, and LK, are labeled in the figure. River channels are marked with blue lines.

the findings of this study were supplied by DLR under license and so cannot be made freely available. Requests for access to these data should be made to TanDEM-X Science Coordination, tandemsience@dlr.de. SRTM DEMs used to support the validations of this study have been deposited in CGIAR-CSI SRTM 90m DEM Digital Elevation Database (<http://srtm.csi.cgiar.org/srtmdata/>). The SfM DEM data used to support the findings of this study are available from the corresponding author upon request.

## Conflicts of Interest

The authors declare that there are no conflicts of interest regarding the publication of this paper.

## Acknowledgments

This work was supported by the National Natural Science Foundation of China [41671353, U1303285, 41571363, 41431174, 61471358, 41201346, 41301394, 41301464] and the CAS Knowledge Innovation Program [KZCX2-EW-320].

## References

- [1] X. Xia, F.-b. Wang, and Y. Zhao, *Lop Nur in China*, Science Press, Beijing, China, 2007.
- [2] S. Hedin, *Scientific Results of a Journey in Central Asia*, Lithographic institute of the General staff of the Swedish army [K. Boktryckeriet, PA Norstedt & söner], 1907.
- [3] N. G. Hörner, P. C. Chen, and N. G. Horner, "Alternating lakes, some river changes and lake displacements in central Asia," *Geografiska Annaler*, vol. 17, pp. 145–166, 1935.
- [4] Z. Dong, P. Lv, G. Qian, X. Xia, Y. Zhao, and G. Mu, "Research progress in China's Lop Nur," *Earth-Science Reviews*, vol. 111, no. 1-2, pp. 142–153, 2012.
- [5] C. Reinhardt, B. Wünnemann, and S. K. Krivonogov, "Geomorphological evidence for the Late Holocene evolution and the Holocene lake level maximum of the Aral Sea," *Geomorphology*, vol. 93, no. 3-4, pp. 302–315, 2008.
- [6] P. Micklin, "The past, present, and future Aral Sea," *Lakes & Reservoirs: Research and Management*, vol. 15, no. 3, pp. 193–213, 2010.
- [7] B. Li, L. Ma, P. Jiang et al., "High precision topographic data on Lop Nur basin's Lake "great Ear" and the timing of its becoming a dry salt lake," *Chinese Science Bulletin*, vol. 53, no. 6, pp. 905–914, 2008.
- [8] L. Wang, H. Gong, Y. Shao et al., "Analysis of elevation discrepancies along the Lop Nur ear-shaped stripes observed using GLAS and DGPS data," *International Journal of Remote Sensing*, vol. 35, no. 4, pp. 1466–1480, 2014.
- [9] B. Smith and D. Sandwell, "Accuracy and resolution of shuttle radar topography mission data," *Geophysical Research Letters*, vol. 30, no. 9, pp. 1–20, 2003.

- [10] P. Berry, J. Garlick, and R. Smith, "Near-global validation of the SRTM DEM using satellite radar altimetry," *Remote Sensing of Environment*, vol. 106, no. 1, pp. 17–27, 2007.
- [11] H. I. Reuter, A. Nelson, P. Strobl, W. Mehl, and A. Jarvis, "A first assessment of aster GDEM tiles for absolute accuracy, relative accuracy and terrain parameters," in *Proceedings of the 2009 IEEE International Geoscience and Remote Sensing Symposium, IGARSS 2009*, pp. V240–V243, South Africa, July 2009.
- [12] P. Guth, "Geomorphometric comparison of ASTER GDEM and SRTM," in *Proceedings of the ISPRS Technical Commission IV & AutoCarto in conjunction with ASPRS/CaGIS*, 2010.
- [13] G. Krieger, A. Moreira, H. Fiedler et al., "TanDEM-X: a satellite formation for high-resolution SAR interferometry," *IEEE Transactions on Geoscience and Remote Sensing*, vol. 45, no. 11, pp. 3317–3340, 2007.
- [14] Y. Du, Q. Xu, L. Zhang et al., "Recent landslide movement in Tsaoling, Taiwan tracked by TerraSAR-X/TanDEM-X DEM time series," *Remote Sensing*, vol. 9, no. 4, p. 353, 2017.
- [15] H. Rott, J. Wuite, D. Floricioiu et al., "Synergy of TanDEM-X DEM differencing and input-output method for glacier monitoring," in *Proceedings of the IEEE International Geoscience and Remote Sensing Symposium, IGARSS 2015*, pp. 5216–5219, July 2015.
- [16] M. Rankl and M. Braun, "Glacier elevation and mass changes over the central Karakoram region estimated from TanDEM-X and SRTM/X-SAR digital elevation models," *Annals of Glaciology*, vol. 57, no. 71, pp. 273–281, 2016.
- [17] J. Neelmeijer, M. Motagh, and B. Bookhagen, "High-resolution digital elevation models from single-pass TanDEM-X interferometry over mountainous regions: a case study of Inylchek Glacier, Central Asia," *ISPRS Journal of Photogrammetry and Remote Sensing*, vol. 130, pp. 108–121, 2017.
- [18] J. Schreyer, C. Geiß, and T. Lakes, "TanDEM-X for large-area modeling of urban vegetation height: evidence from Berlin, Germany," *IEEE Journal of Selected Topics in Applied Earth Observations and Remote Sensing*, vol. 9, no. 5, pp. 1876–1887, 2016.
- [19] J. Schreyer and T. Lakes, "Deriving and evaluating city-wide vegetation heights from a TanDEM-X DEM," *Remote Sensing*, vol. 8, no. 11, p. 940, 2016.
- [20] J. Kubanek, J. A. Richardson, S. J. Charbonnier, and L. J. Connor, "Lava flow mapping and volume calculations for the 2012–2013 Tolbachik, Kamchatka, fissure eruption using bistatic TanDEM-X InSAR," *Bulletin of Volcanology*, vol. 77, no. 12, p. 106, 2015.
- [21] F. Albino, B. Smets, N. D'Oreye et al., "High-resolution TanDEM-X DEM: An accurate method to estimate lava flow volumes at Nyamulagira Volcano (D. R. Congo)," *Journal of Geophysical Research: Solid Earth*, vol. 120, no. 6, pp. 4189–4207, 2015.
- [22] S. Zwieback, A. Bartsch, J. Boike et al., "Monitoring permafrost and thermokarst processes with TanDEM-X DEM time series: Opportunities and limitations," in *Proceedings of the 36th IEEE International Geoscience and Remote Sensing Symposium, IGARSS 2016*, pp. 332–335, July 2016.
- [23] A. Gruber, B. Wessel, M. Huber, and A. Roth, "Operational TanDEM-X DEM calibration and first validation results," *ISPRS Journal of Photogrammetry and Remote Sensing*, vol. 73, pp. 39–49, 2012.
- [24] P. Rizzoli, B. Bräutigam, T. Kraus, M. Martone, and G. Krieger, "Relative height error analysis of TanDEM-X elevation data," *ISPRS Journal of Photogrammetry and Remote Sensing*, vol. 73, no. 6, pp. 30–38, 2012.
- [25] N. Yague-Martinez, C. Rossi, M. Lachaise, F. Rodriguez-Gonzalez, T. Fritz, and H. Breit, "Interferometric processing algorithms of TanDEM-X data," in *Proceedings of the 2010 30th IEEE International Geoscience and Remote Sensing Symposium, IGARSS 2010*, pp. 3518–3521, July 2010.
- [26] R. M. Goldstein and C. L. Werner, "Radar interferogram filtering for geophysical applications," *Geophysical Research Letters*, vol. 25, no. 21, pp. 4035–4038, 1998.
- [27] M. Costantini, "A novel phase unwrapping method based on network programming," *IEEE Transactions on Geoscience and Remote Sensing*, vol. 36, no. 3, pp. 813–821, 1998.
- [28] O. H. Sahraoui, B. Hassaine, C. Serief et al., "Radar interferometry with sarscape software," *Photogrammetry and Remote Sensing*, 2006.
- [29] A. Schubert, M. Jehle, D. Small et al., "Geometric validation of TerraSAR-X high-resolution products," in *Proceedings of the 3rd TerraSAR-X Sci Team Meeting*, pp. 25–26, 2008.
- [30] J. Hueso González, J. M. Walter Antony, M. Bachmann et al., "Bistatic system and baseline calibration in TanDEM-X to ensure the global digital elevation model quality," *ISPRS Journal of Photogrammetry and Remote Sensing*, vol. 73, pp. 3–11, 2012.
- [31] J. Gonzalez, M. Bachmann, G. Krieger et al., "Development of the TanDEM-X calibration concept: analysis of systematic errors," *IEEE Transactions on Geoscience and Remote Sensing*, vol. 48, no. 2, pp. 716–726, 2010.
- [32] B. Wessel, A. Bertram, A. Gruber et al., "A new high-resolution elevation model of Greenland derived from TanDEM-X," *ISPRS Annals of Photogrammetry, Remote Sensing & Spatial Information Sciences*, vol. 3, no. 7, 2016.
- [33] W. Lee, H. Jung, and Z. Lu, "Application of ERS and Envisat cross-interferometry to generation and accuracy assessment of digital elevation model over northern Alaska," *Journal of Applied Remote Sensing*, vol. 9, no. 1, p. 096065, 2015.
- [34] H. Zwally, B. Schutz, W. Abdalati et al., "ICESat's laser measurements of polar ice, atmosphere, ocean, and land," *Journal of Geodynamics*, vol. 34, no. 3–4, pp. 405–445, 2002.
- [35] J. B. Abshire, X. Sun, H. Riris et al., "Geoscience Laser Altimeter System (GLAS) on the ICESat mission: On-orbit measurement performance," *Geophysical Research Letters*, vol. 32, no. 21, pp. 1–4, 2005.
- [36] H. A. Fricker, A. Borsa, B. Minster et al., "Assessment of ICESat performance at the salar de Uyuni, Bolivia," *Geophysical Research Letters*, vol. 32, no. 21, 2005.
- [37] C. F. Martin, R. H. Thomas, W. B. Krabill et al., "ICESat range and mounting bias estimation over precisely-surveyed terrain," *Geophysical Research Letters*, vol. 32, no. 21, pp. 1–4, 2005.
- [38] G. Li, X. Tang, C. Zhang, X. Gao, and J. Chen, "Multi-criteria constraint algorithm for selecting ICESat/GLAS data as elevation control points," *Journal of Remote Sensing*, vol. 21, no. 1, pp. 96–104, 2017.
- [39] J. Li, C. Fan, Y. Chu, and S. Zhang, "Using ICESAT altimeter data to determine the Antarctic ice sheet elevation model," *Geomatics and Information Science of Wuhan University*, vol. 33, no. 3, pp. 226–228, 2008.
- [40] N. K. Pavlis, S. A. Holmes, S. C. Kenyon et al., "An earth gravitational model to degree 2160: EGM2008," *EGU General Assembly*, vol. 10, pp. 13–18, 2008.
- [41] N. K. Pavlis, S. A. Holmes, S. C. Kenyon et al., "The development and evaluation of the Earth Gravitational Model 2008 (EGM2008)," *Journal of Geophysical Research: Solid Earth*, vol. 117, no. 4, pp. 1978–2012, 2012.

- [42] A. Lucieer, D. Turner, D. H. King et al., "Using an unmanned aerial vehicle (UAV) to capture micro-topography of Antarctic moss beds," *International Journal of Applied Earth Observation and Geoinformation*, vol. 27, pp. 53–62, 2014.
- [43] A. Lucieer, S. M. D. Jong, and D. Turner, "Mapping landslide displacements using Structure from Motion (SfM) and image correlation of multi-temporal UAV photography," *Progress in Physical Geography*, vol. 38, no. 1, pp. 97–116, 2014.
- [44] L. Wallace, A. Lucieer, Z. Malenovsky et al., "Assessment of forest structure using two UAV techniques: a comparison of airborne laser scanning and structure from motion (SfM) point clouds," *Forests*, vol. 7, no. 3, p. 62, 2016.
- [45] F. Mancini, M. Dubbini, M. Gattelli, F. Stecchi, S. Fabbri, and G. Gabbianelli, "Using unmanned aerial vehicles (UAV) for high-resolution reconstruction of topography: The structure from motion approach on coastal environments," *Remote Sensing*, vol. 5, no. 12, pp. 6880–6898, 2013.
- [46] A. Stein, *Serindia: Detailed Report of Archaeological Explorations in Central Asia and Westernmost China*, Oxford, UK, 1921.
- [47] K. Johnson, E. Nissen, S. Saripalli et al., "Rapid mapping of ultrafine fault zone topography with structure from motion," *Geosphere*, vol. 10, no. 5, pp. 969–986, 2014.
- [48] M. Werner, "Shuttle radar topography mission (SRTM) mission overview," *Frequenz*, vol. 55, no. 3-4, pp. 75–79, 2001.
- [49] J. J. van Zyl, "The shuttle radar topography mission (SRTM): a breakthrough in remote sensing of topography," *Acta Astronautica*, vol. 48, no. 5-12, pp. 559–565, 2001.
- [50] E. Rodríguez, C. S. Morris, and J. E. Belz, "A global assessment of the SRTM performance," *Photogrammetric Engineering and Remote Sensing*, vol. 72, no. 3, pp. 249–260, 2006.
- [51] M. Martone, P. Rizzoli, and G. Krieger, "Volume decorrelation effects in TanDEM-X interferometric SAR data," *IEEE Geoscience and Remote Sensing Letters*, vol. 13, no. 12, pp. 1812–1816, 2016.
- [52] T. Fritz, U. Bals, R. Bamler et al., "Phase unwrapping correction with dual-baseline data for the TanDEM-X mission," in *Proceedings of the Geoscience and Remote Sensing Symposium*, pp. 5566–5569, 2012.



**Hindawi**

Submit your manuscripts at  
[www.hindawi.com](http://www.hindawi.com)

